Multicellular natural convection in a high aspect ratio cavity: experimental and numerical results

Bérengère Lartigue*, Sylvie Lorente, Bernard Bourret

Laboratoire d'Etudes Thermiques Et Mécaniques, Institut National des Sciences Appliqueés, 135 Avenue de Rangueil, 31077 Toulouse cedex 4, France

Abstract

This work is a contribution to the highlighting of the secondary flows in vertical cavities with high aspect ratio, in laminar regime. Multicellular flows in high aspect ratio two-dimensional cavities, such as those encountered in insulated glazing units, are the main focus of this investigation. Numerical and experimental results are presented. Authors investigate a numerical study on the temperature field and the associated Nusselt number, and on the velocity field. In the experiments, Particle Image Velocimetry is used to obtain the velocity field. The numerical and experimental results show the presence of secondary cells. © 2000 Elsevier Science Ltd. All rights reserved.

1. Introduction

Convective heat transfer is a major parameter in the total heat exchange observed in insulated glazing units (IGU). These IGU generally consist of two panes of glass of height H spaced apart by a certain distance L. The resulting aspect ratio ($A = H/L$) is generally greater than 15. The sealed guide ensures the sealing of the cell. Fluid movement in the cavity is due to buoyancy forces resulting from a temperature difference between both vertical surfaces. The flow is generally laminar and unicellular, with the fluid rising near the warm surface and descending near the cold one. There are, however, situations, always in the laminar regime, in which secondary cells appear in the cavity core. The flow, multicellular in this case, tends to increase local and average heat transfer coefficients.

Bejan presents the basis of convective heat transfer in [1]. Theoretical and numerical studies performed by Raithby and Wong [2], de Vahl Davis [3], Korpela et al. [4] refined the resolution of the problem. These studies point out that the solution is a function of three dimensionless parameters which are the aspect ratio of the cavity A, the Prandtl number of the fluid Pr and the Rayleigh number Ra.

In the last few years, many researchers are learning on the particular study of the flows in high rectangular cavities, which characterize the transfers in double glazing. The specific problem of multicellular flow was discovered by Elder [5], who observed, in experimental studies, a secondary flow pattern attributable to hydrodynamic instability. Several numerical models have been able to resolve secondary cells in a vertical slot. Some authors point out that the onset of secondary cells can be delayed by the false diffusion resulting from numerical upwinding schemes. Others use a central difference discretization scheme and uniform grids [6–11]. Lee and Korpela [6] found the expression of critical value of the Grashof number ($Gr = Ra/Pr$) at which the onset of secondary cells takes place. Some authors determine the number of cells in the center

* Corresponding author.

Nomenclature

A	aspect ratio $A = H/L$
g	acceleration due to gravity, m/s^2
Gr	Grashof number $Gr = Ra/Pr$
h	convective heat transfer coefficient, W/(m^2 K)
H	height of air layer, m
l_c	vertical dimension of a cell, m
L	thickness of air layer, m
n_c	number of cells
Nu	Nusselt number
Nu_L	Nusselt number based on cavity thickness
p	pressure, Pa
P	dimensionless pressure
Pr	Prandtl number $Pr = \nu/\kappa$
Ra	Rayleigh number $Ra = g\beta\Delta T L^3/\nu\kappa$
t	time, s
t^*	dimensionless time
T	temperature, K
u, w	x-component and z-component of velocity, m/s
U, W	dimensionless x-component and z-component

	of velocity
V_0	dimensionless reference velocity $V_0 = \sqrt{g\beta\Delta T L}$
x, z	Cartesian coordinates
X, Z	dimensionless Cartesian coordinates
α_c	wave number of cells
β	thermal volumetric expansion coefficient, K^{-1}
ΔT	temperature difference, $\Delta T = T_h - T_c$, K
$\Phi(z)$	local heat flow, W/m^2
κ	thermal diffusivity, m^2/s
λ	thermal conductivity, W/(m K)
ν	kinematic viscosity, m^2/s
ρ	density, kg/m^3
θ	dimensionless temperature

Subscripts

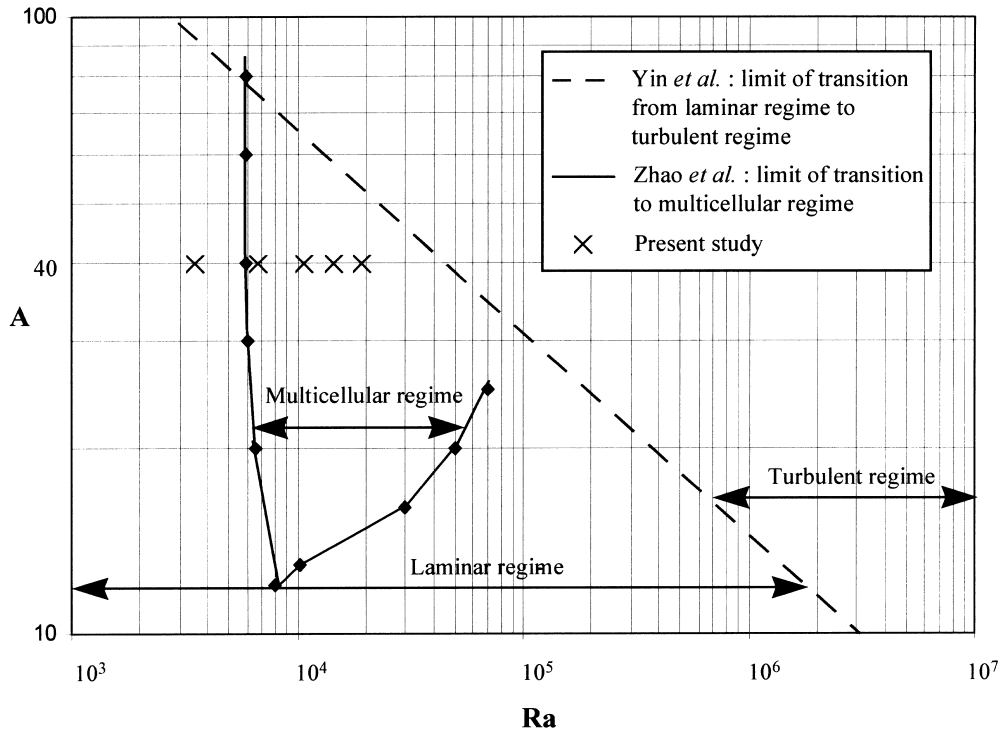|	
c	cold
h	hot
m	mean
0	reference

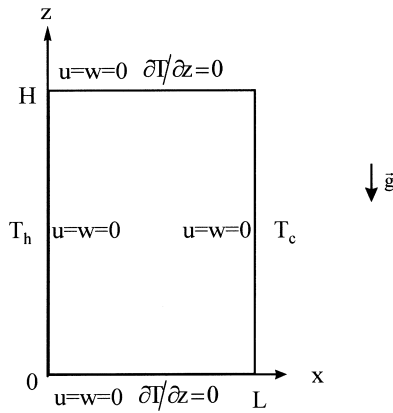
Fig. 1. Flow regime definitions.

Fig. 2. Geometry and boundary conditions.

region according to the Rayleigh number [6,10,12]. More recently, Wright and Sullivan [13] performed a literature review on natural convection in IGU. Works by Zhao et al. [14] made it possible to lead to a good knowledge of multicellular flows appearing in laminar regime. Their study provided a 'map' of appearance of the cells for several values of Rayleigh number and aspect ratio (see Fig. 1).

As can be seen the scientific literature contains a number of numerical studies references. There is, however, a paucity of information on experimental studies highlighting secondary flow in laminar regime. The aim of this article is to provide experimental results showing the existence of a 'cats-eye' pattern in laminar flow. Experiments were carried out using the Particle Image Velocimetry (PIV) technique which enables the analysis of the velocity field. In parallel with this work, a numerical study, also presented in this article, was undertaken.

2. Description of the computer code

Fig. 2 presents the geometry and the boundary conditions of a two-dimensional (2D) rectangular enclosure. The laminar fill gas flow can be described by assuming that the fluid is Newtonian and satisfies the Boussinesq approximation. The air flow in the cavity is governed by the laws of conservation of mass, momentum and energy. These equations can be put into dimensionless forms using the following dimensionless variables:

$$X = \frac{x}{L} \quad Z = \frac{z}{L} \quad A = \frac{H}{L}$$

$$U = \frac{u}{V_0} \quad W = \frac{w}{V_0} \quad \text{with } V_0 = \sqrt{g\beta\Delta T L}$$

$$P = \frac{p}{\rho V_0^2} \quad \theta = \frac{T - T_m}{T_h - T_c} = \frac{T - T_m}{\Delta T} \quad \text{with}$$

$$T_m = \frac{T_h + T_c}{2}$$

$$t^* = \frac{t}{t_0} \quad \text{with } t_0 = \frac{L}{V_0} = \frac{L}{\sqrt{g\beta\Delta T L}} = \frac{\sqrt{L}}{\sqrt{g\beta\Delta T}}$$

The governing equations can therefore be written in the following dimensionless forms:

$$\frac{\partial U}{\partial X} + \frac{\partial W}{\partial Z} = 0 \tag{1}$$

$$\frac{\partial U}{\partial t^*} + U\frac{\partial U}{\partial X} + W\frac{\partial U}{\partial Z}$$
$$= -\frac{\partial P}{\partial X} + \left(\frac{Pr}{Ra}\right)^{1/2}\left(\frac{\partial^2 U}{\partial X^2} + \frac{\partial^2 U}{\partial Z^2}\right) \tag{2}$$

$$\frac{\partial W}{\partial t^*} + U\frac{\partial W}{\partial X} + W\frac{\partial W}{\partial Z}$$
$$= -\frac{\partial P}{\partial Z} + \left(\frac{Pr}{Ra}\right)^{1/2}\left(\frac{\partial^2 U}{\partial X^2} + \frac{\partial^2 U}{\partial Z^2}\right) + \theta \tag{3}$$

$$\frac{\partial \theta}{\partial t^*} + U\frac{\partial \theta}{\partial X} + W\frac{\partial \theta}{\partial Z}$$
$$= (Ra \cdot Pr)^{-1/2}\left(\frac{\partial^2 \theta}{\partial X^2} + \frac{\partial^2 \theta}{\partial Z^2}\right) \tag{4}$$

The boundary conditions of velocity and temperature become:

$$U = W = 0 \quad \text{at } X = 0, X = 1 \text{ and } Z = 0, Z = A \tag{5}$$

$$\theta = 0.5 \quad \text{at } X = 0 \tag{6}$$

$$\theta = -0.5 \quad \text{at } X = 1 \tag{7}$$

$$\frac{\partial \theta}{\partial Z} = 0 \quad \text{at } Z = 0, Z = A \tag{8}$$

The resolution of Eqs. (1)–(4) was carried out using a commercially-available computer code called ESTET[1] (Ensemble de Simulations Tridimensionnelles d'Ecoulements Turbulents). ESTET resolves equations of fluid mechanics discretized in structured grid which uses finite volumes and finite differences. Grid independence checks (not presented in this article) were performed.
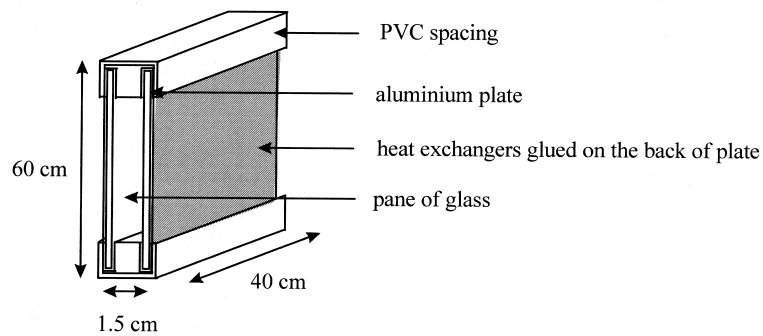
(a)
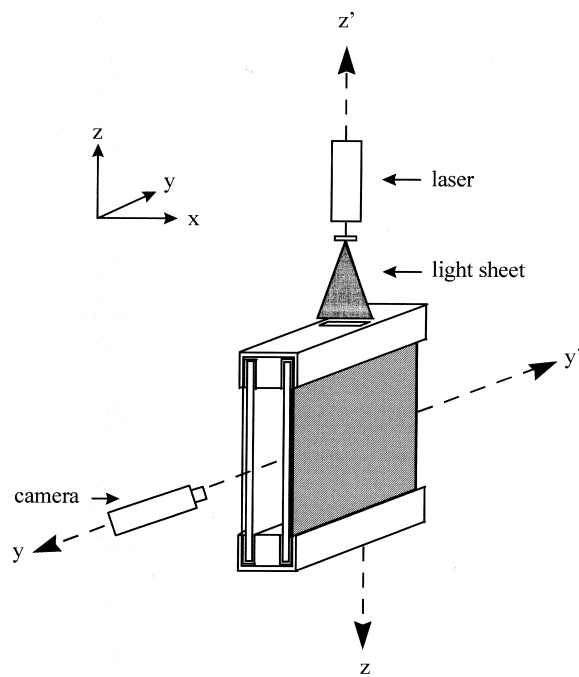
(b)

Fig. 3. Schematic of apparatus (a) and experimental set-up (b).

These checks revealed that approximately 30,000 grid nodes were necessary to obtain a grid independent solution. To ensure the convergence of calculation, it is indeed imperative to place the first nodes in the viscous layer of the walls, which is the zone of greatest temperature gradients. That is the reason why the first nodes are spaced of a dimensionless thickness of 0.02. The following boundary conditions are imposed: a condition of nonslip, impermeability and adiabatic transfer in the top and bottom of the cavity, and a condition of nonslip and impermeability on the vertical walls.

3. Experimental set-up

The experimental apparatus and the Particle Image Velocimetry (PIV) set-up are shown schematically in Fig. 3.
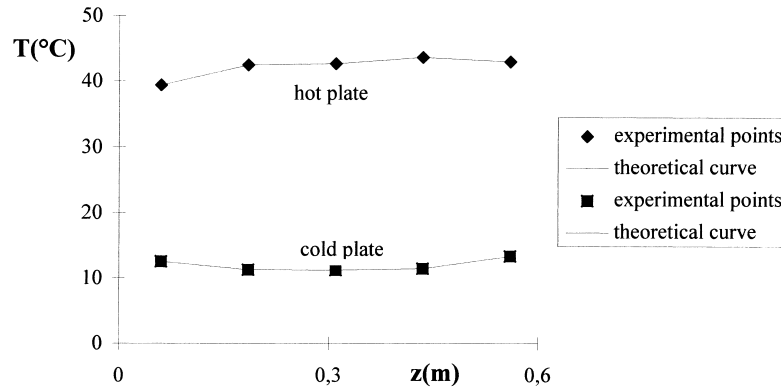
Fig. 4. Experimental and theoretical temperatures along hot and cold faces.

3.1. Experimental apparatus

The apparatus is a parallelepipedic closed cavity, filled with air, with a height of $H = 60$ cm. The main vertical plates are made of aluminium to favor isothermicity. The two other vertical plates are made of glass so as to visualize the laser sheet of the PIV. The bottom and top horizontal plates are made of PVC to limit thermal bridge. The plates spacing used is $L = 1.5$ cm, resulting in aspect ratio of $A = 40$ (see Fig. 3(a)). A zero heat flux boundary condition is very difficult to reach from an experimental point of view. Nevertheless, considering the works of Raithby and Wong [2], if the aspect ratio is important enough ($A \geq 40$), the influence of the horizontal boundary conditions (perfectly adiabatic or perfectly conducting) on the Nusselt number is small.

The temperatures of the aluminium plates are regulated by heat exchangers made of rubber pipes which are glued on the back of the plates. Water and refrigerant circulate in the heat exchangers to maintain desired conditions. However, it's difficult to obtain isothermal walls. Therefore, the exact temperature along the plates was measured using 18 probes glued on each plate. A law of variation of surface temperature vs. height was then deduced from measurements and became the thermal boundary condition in numerical study (see Fig. 4). Considering physical properties of air at $T_m = (T_h + T_c)/2$ the Rayleigh number of the experiment is $Ra = 9222$.

3.2. PIV technique

The PIV system is based on the single relation velocity = distance/time. Thus, the measure of the travelling distance of a fluid particle in a given time interval gives the velocity. Therefore, it is necessary to seed the flow with small tracer particles of same density as air, which travel with the flow, and that can be visualized. Incense smoke was chosen as seeding material. When a 2D slice of the flow field is illuminated by a light sheet in the middle of the cavity, as shown on Fig. 3(b), the illuminated seeding scatters this light and is detected by a camera placed at right angle to the light sheet. Two camera images are recorded, the first showing the initial position of the seeding particles, and the second their final position due to the movement of the flow field. The time between the recording images is known.

The two camera frames are then processed to find the velocity vector map of the flow field. They are divided into smaller regions that are considered individually. Correlation and Fourier transform methods are used to measure the average displacement of the ensemble of particles in a region. The fluid velocity is then calculated over the time interval between the successive images. This is repeated for each region and so the whole 2D velocity vector map is built-up. One hundred velocity vector maps are realized, each second.

Dimensions of a measure area are 3×3 cm. Therefore, about twenty areas are necessary to cover the apparatus height; then, about 2000 data files have to be treated before reaching the velocity field in the whole cavity.

4. Results and discussion

It's noteworthy that the vertical faces are isothermal in each simulation, except when the point is to compare experimentation to numerical results where, in this case, experimental data become boundary conditions for simulation.
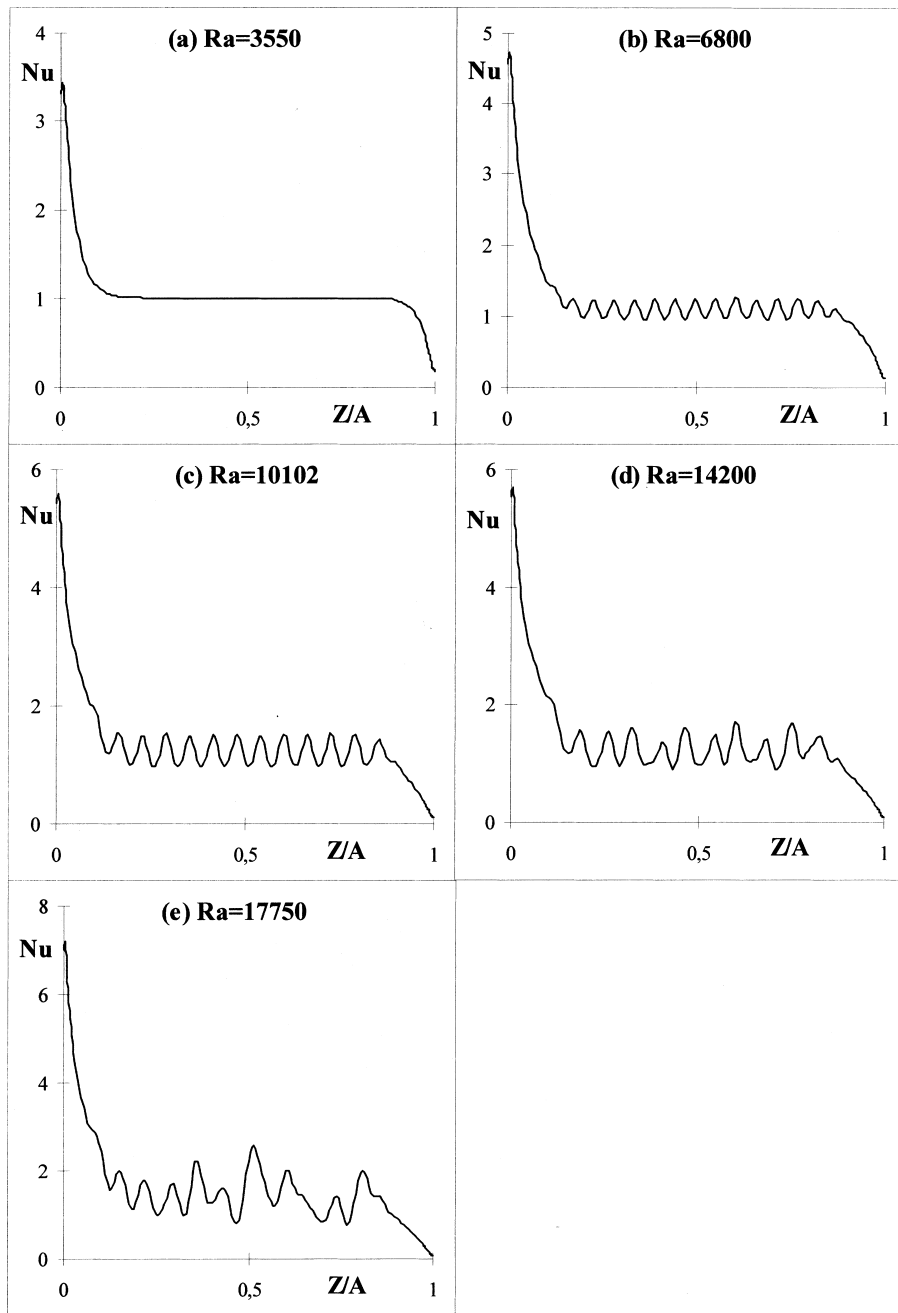
Fig. 5. Evolution of local Nusselt number *Nu* vs. dimensionless height Z/A for $A = 40$ and several *Ra*.

4.1. Temperature field

The thermal field in the cavity is obtained numerically. Nusselt number is calculated in order to evaluate the rate of heat transfer across the enclosure. Local Nusselt numbers which represent the ratio of convec-

tive heat transfer over conductive heat transfer, are calculated according to Eqs. (9) and (10):

$$Nu(z) = \frac{h(z)x}{\lambda(z)} \qquad (9)$$

Table 1
Average Nusselt numbers

Ra	Present study (numerical)	Zhao et al. (numerical)	Wright et al. (numerical)	Lee et al. (numerical)	ElSherbiny et al. (experimental)
3550	1.064	1.063	Not available	1.05	1.009
6800	1.167	1.158	1.15	Not available	1.096
10,102	1.292	1.277	1.28	Not available	1.244
14,200	1.388	1.399	Not available	1.38	1.417
17,750	1.484	1.487	Not available	1.46	1.549

and

$$h(z) = \frac{\Phi(z)}{T_h - T_c} = \frac{1}{T_h - T_c} \lambda(T) \frac{T_h - T(x, z)}{x} \qquad (10)$$

where $\Phi(z)$ is the parietal local flow calculated on the hot face at $X = 0.02$, i.e. in the viscous layer. The value of λ is evaluated locally along the vertical wall according to the temperature. The aspect ratio used for all the simulations presented is fixed at $A = 40$, representative of physical reality. Fig. 5(a)–(e) represents the evolution of the local Nusselt number along the hot wall vs. the dimensionless height, for Rayleigh numbers varying from 3550 to 17,750, (the Ra values were chosen in order to compare results obtained with the literature). If the Rayleigh number is equal to 3550, the flow is in the conduction regime. The Nusselt number is then equal to 1 over the height of the cavity, except close to the horizontal walls. If the Rayleigh number increases to about 6000, the flow becomes multicellular. The flow is the seat of instabilities which Fig. 5(b) makes it possible to highlight. Thus, for $Ra = 6800$, the local Nusselt number tends to oscillate on a regular way around the value corresponding to the conduction regime. The same evolution is observed for $Ra = 10,102$, which closely corresponds to the experimental conditions. However if the oscillations remain regular, their amplitude grows and the average Nusselt number is now higher than 1. If the value of Rayleigh number increases further (see Fig. 5(d) and (e)), the regularity of the oscillations is destroyed, the multicellular laminar flow being fully established, before becoming turbulent.

From the knowledge of the local Nusselt number, the average Nusselt number can be calculated by integration of the local values with the height of the cavity. The results obtained are presented in Table 1, where a comparison is made with results available elsewhere in the literature [6,10,14,15]. The values of the present article are closed with the other results. Indeed, a maximum variation of 1.5 and 6% is observed with other numerical studies and with the experimental work of ElSherbiny et al. [15], respectively.

The variation of non-dimensioned temperature in the center of the cavity was also studied. Fig. 6 shows the evolution of dimensionless temperature with dimensionless height. These profiles relate to the aspect ratio $A = 40$ and various values of the Rayleigh number. These temperature profiles allow to put in evidence the onset of the secondary cells. Until $Ra = 6000$, the flow remains unicellular (see Fig. 6(a)). After this limit, named lower limit critical Rayleigh number by some authors [14], the beginning of a secondary flow disturbs the temperature profile in the cavity core. As Ra increases, the temperature profiles are the seat of initially regular oscillations whose width increases with Rayleigh number, until becoming irregular.

4.2. Velocity field

This paragraph is dedicated to the numerical and experimental results obtained on the velocity field. Until now, and to our knowledge, only experimental results on the temperature field were presented in the literature. Thus, instabilities in laminar flow could have been highlighted only with experimental results on temperature. The study carried out here describes the results obtained using a non-intrusive method of measure: the Particle Image Velocimetry.

Fig. 7 plots numerical streamlines in the cavity for Rayleigh numbers ranging from 3550 to 17,750. For a Rayleigh number of 3550, no fluctuation is observed, meaning that the flow is unicellular. When the Rayleigh number increases, the stream patterns begin to fluctuate indicating the onset of the instability, and the

Table 2
Number of cells obtained in different simulations as a function of Ra

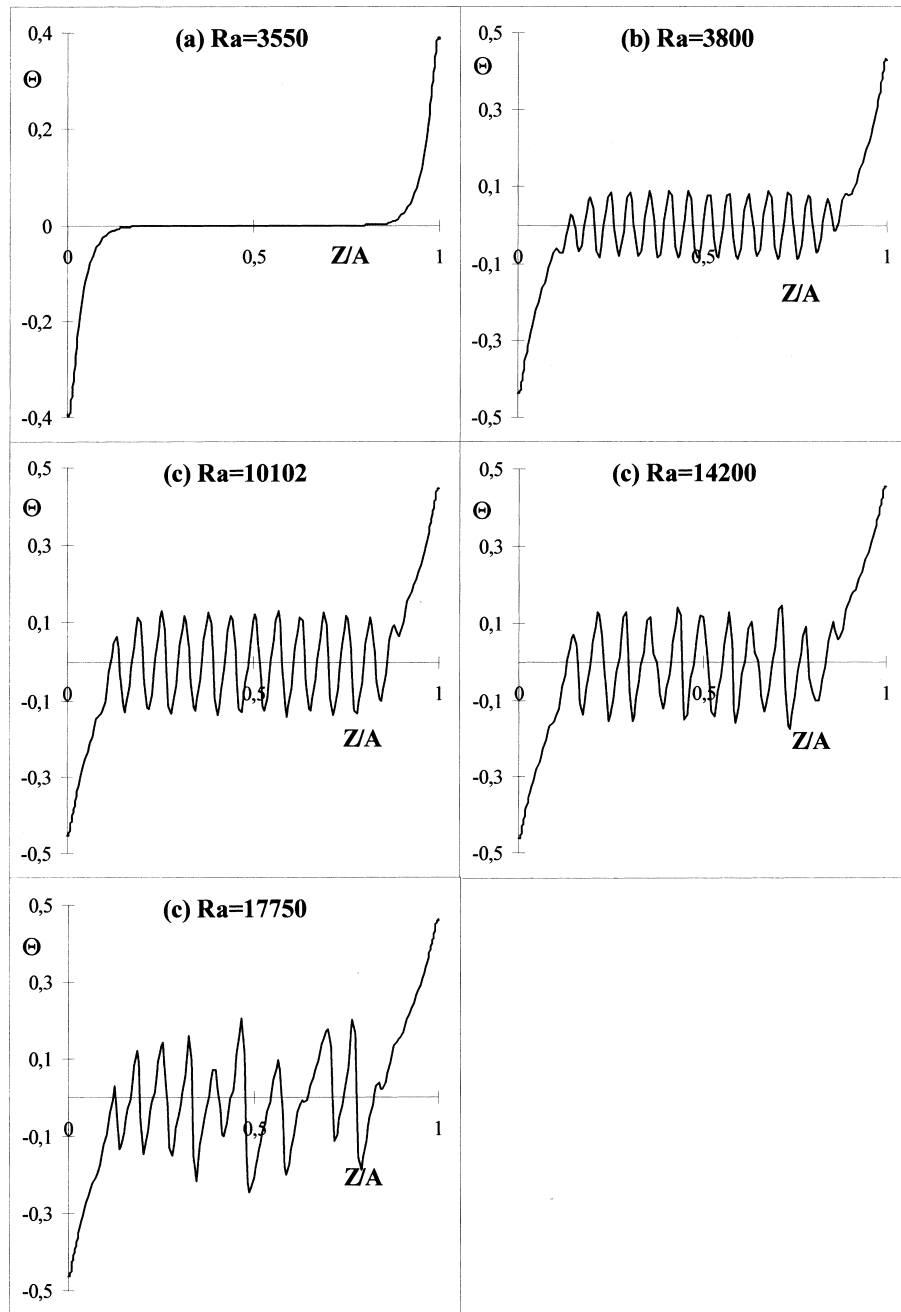| Ra	Present study	References
6800	16	15 [10]
10,102	14	14 [10]
14,200	13	13 [6]
17,750	11	13 [6]

Fig. 6. Evolution of dimensionless temperature θ vs. dimensionless height Z/A for $A = 40$ and several Ra.

flow becomes multicellular. Our numerical results are compared to those available in other papers, in particular using the number of cells existing in the secondary flow. Table 2 lists the number of cells obtained in the simulations of previous authors [6,10] and ones of the present study. These data show that the number of cells decreases as the Rayleigh number increases. Wright and Sullivan [10] expressed this number n_c using Eq. (11):

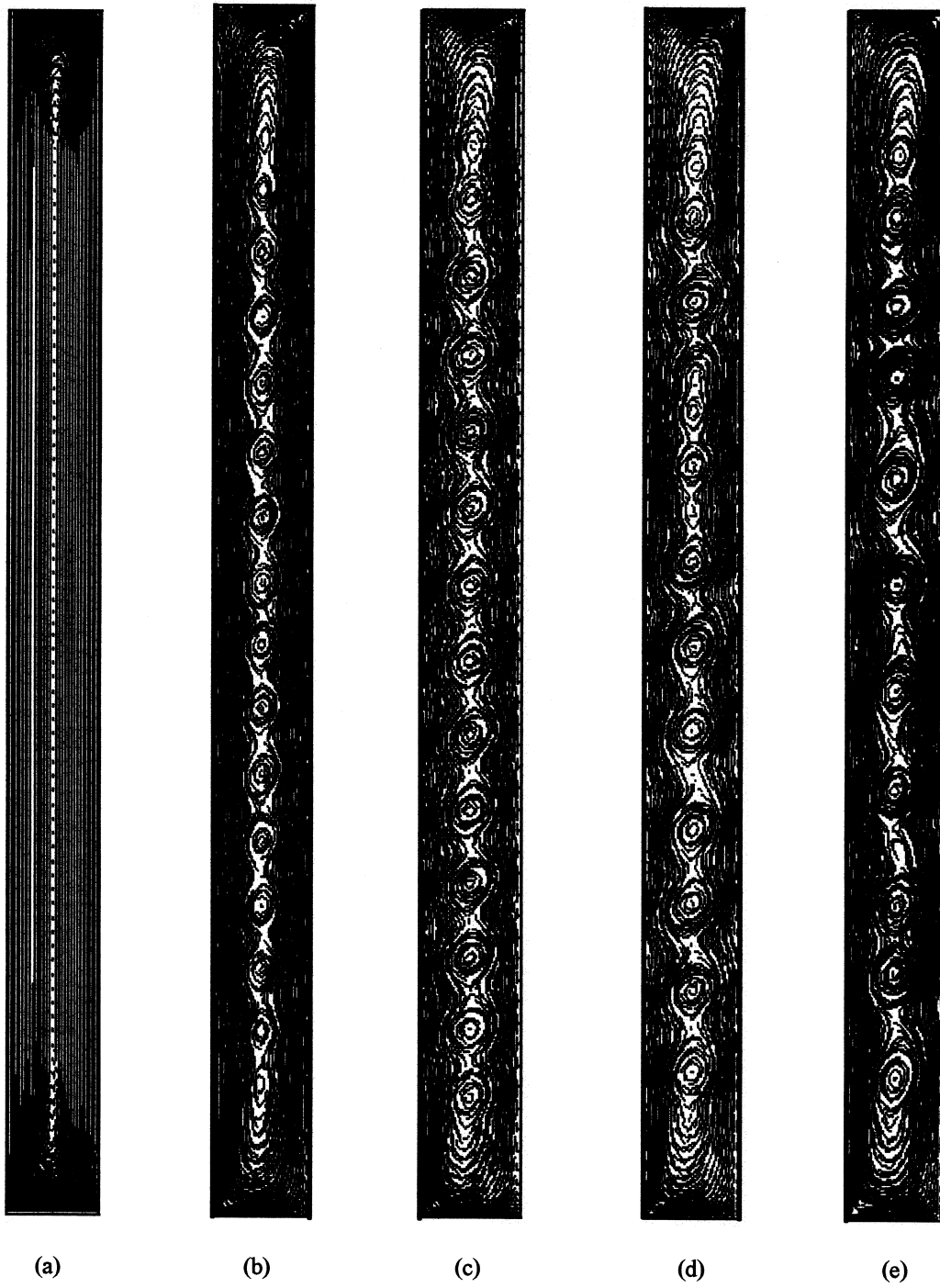$$n_c = \text{int}\left[\frac{A - 10}{2\pi/\alpha_c}\right] + 2 \tag{11}$$

Fig. 7. Numerical streamlines for $A = 40$: (a) $Ra = 3550$, (b) $Ra = 6800$, (c) $Ra = 10,102$, (d) $Ra = 14,200$, (e) $Ra = 17,750$.

Table 3
Wave number for different Grashof numbers [6]

α_c	Gr
2.82	11,000
2.78	12,000
2.5	15,000
2.41	20,000
2.33	25,000

α_c, the non-dimensional wave number, is calculated by interpolating numerical data presented by Lee and Korpela [6] (see Table 3).

Figs. 8 and 9 represent, in steady state, non-dimensioned horizontal and vertical components of velocity in experimental and numerical cases. The choice of this representation is justified by the following reason: if the stream function ends in an immediate observation of the cells in the secondary flow, the layout of the velocity vector components makes it possible to quantify the velocity of the cells compared to the one of the primary flow.

The cavity is divided in two different zones: the top and bottom (see Fig. 8) and the cavity core (see Fig. 9). First, Fig. 8 presents experimental and numerical results, in high (a) and low (b) part of the cavity. A very good agreement between experimental and numerical values is found for the two representations. Experimentation and simulation show that primary flow is carried out from the hot face towards the cold face along the top horizontal plate. It is the reverse close to the horizontal plate in the low part of the enclosure.

Then, the cavity core represents a zone ranging from around $Z/A = 0.15$ to $Z/A = 0.85$ (see Fig. 9). Non-dimensioned horizontal and vertical components of the velocity vector are presented here for several heights of measure area: $Z/A = 0.15$, $Z/A = 0.35$, $Z/A = 0.50$ and $Z/A = 0.80$ approximately. In this case as well, experimental and numerical values of velocity are closed. It should be specified that, on these figures, the cold face is left side and the hot face is on the right. Two zones of same intensity and opposed direction of component U coupled with the component W indicate the presence of a cell. Thus, from the results obtained, one can note that the velocity of a secondary cell is quasi reduced to its horizontal component in the centerline of the cavity ($X = 0.5$) and its average value represents 13% of the velocity in the primary flow. Fig. 9(a) shows the existence of two half cells in this area. The horizontal component of the velocity is directed cold face towards hot face, in the low part of the cell; approaching the hot boundary layer, the vertical component, ascending, prevails. It is the reverse in the upper part of the cell, where the horizontal component is directed towards the cold face. Close to the cold boundary layer, the velocity vector is reduced to its downward vertical component. Consequently, the rotation of the secondary cell is in this case, anticlockwise. Thus, experimental and numerical results make it possible to highlight the existence of secondary cells and their rotation.

Besides the rotary movement, the analysis of the various recordings of the velocity field put the stress on a global displacement of the secondary cells. The average velocity field was then studied. Fig. 10 rep-
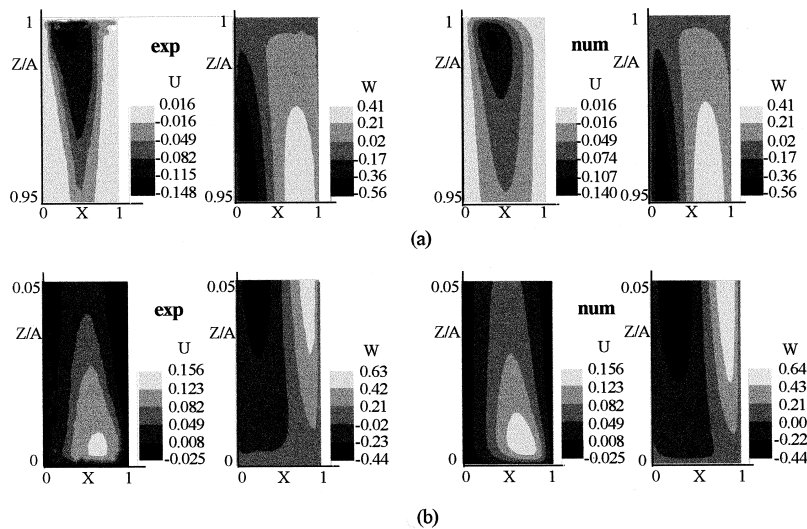

Fig. 8. Non-dimensioned horizontal and vertical components of velocity in experimental (exp) and numerical (num) cases: (a) top, (b) bottom.
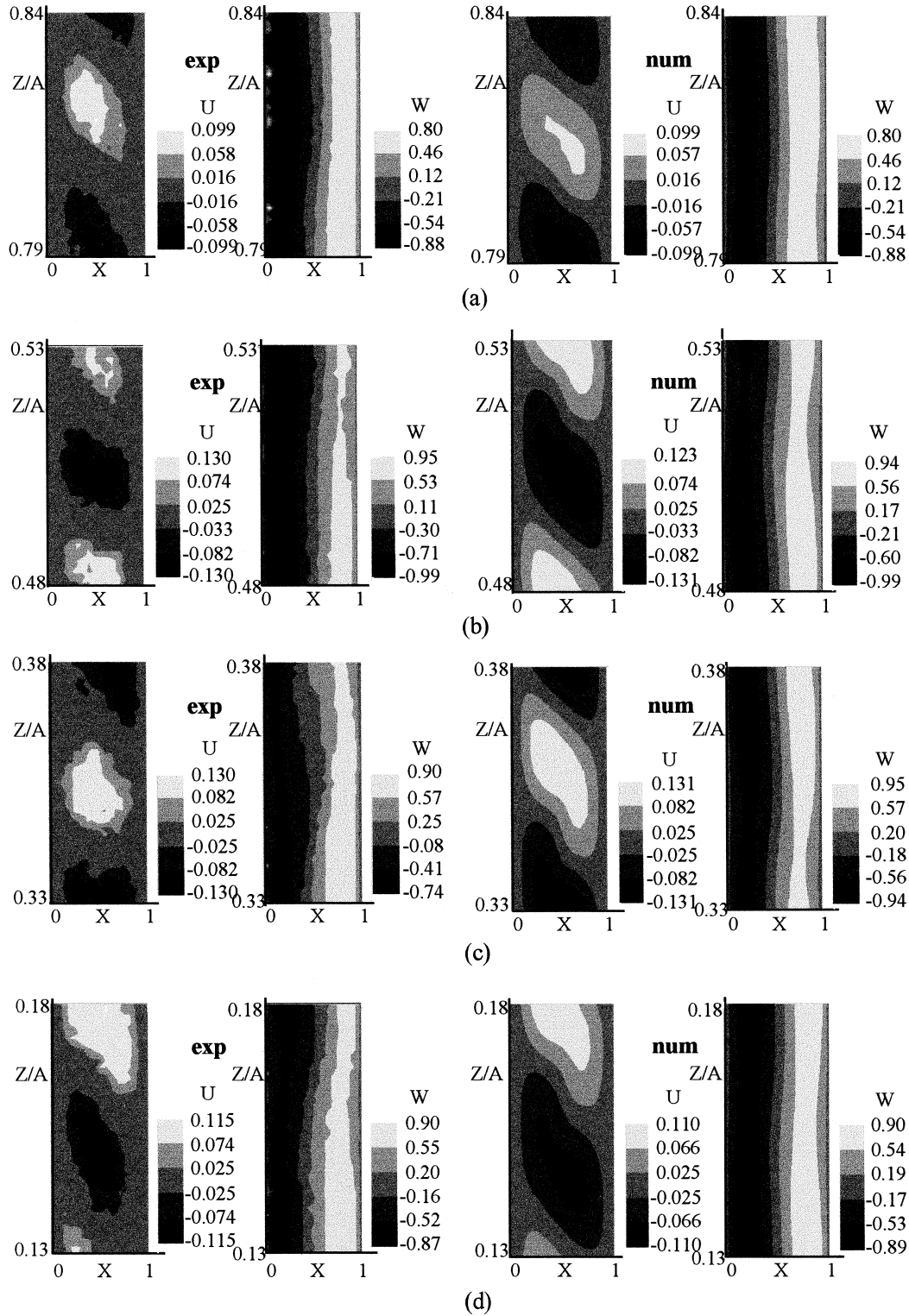
Fig. 9. Non-dimensioned horizontal and vertical components of velocity in experimental (exp) and numerical (num) cases in the core of the cavity.
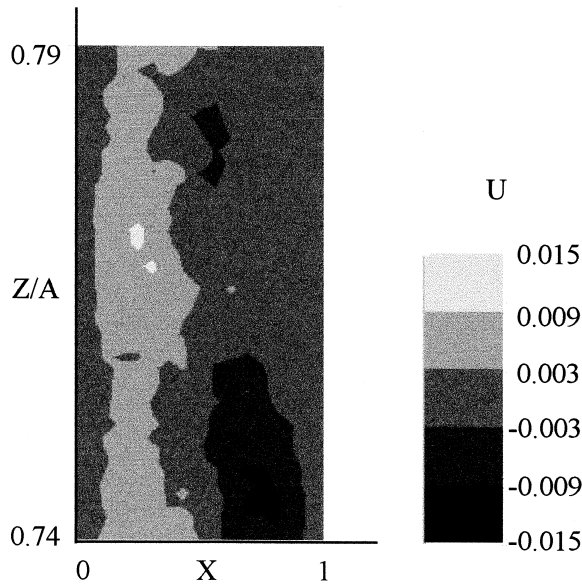
Fig. 10. Average non-dimensioned component U during a non-dimensioned time of 810 in a measure area.

resents the experimental average value of the dimensionless horizontal component U calculated during a dimensionless time of 810. It can be noticed that U is practically equal to 0, which means that the secondary flow velocity field is dynamic: the cells do not remain stationary. In the same way, Fig. 11 represents numerical dimensionless component U evolution vs. dimensionless time t^*, in the center point of the area defined by $Z/A = 0.74$ to $Z/A = 0.79$, i.e. $X = 0.5$ and $Z/A = 0.765$. Evolution is sinusoidal, with a non-dimensioned period of 275. As well as in experimental study, the

average value of U during a dimensionless time of 810 is null. This periodic evolution demonstrates the global movement of cells.

Figs. 12 and 13 represent in a same area, respectively non-dimensioned experimental and numerical component U, for a significant non-dimensioned step of time of 32.4 (i.e., 4 s). Spatial evolution can be observed. Considering that the center of the cell is located between two zones of opposed values of U, an average displacement velocity of the cell can be reached. The non-dimensioned values of this average velocity are 0.0107 for experience and 0.0110 for numerical study, which represents about the hundredth of the maximum value of velocity near the plates. Related to the boundary conditions imposed, the secondary cells seem to move in the direction of the bottom of the enclosure.

Fig. 14 shows the horizontal velocity profile in the cavity core ($X = 0.5$) according to the height. The velocity profile plotted in this example concerns dimensionless height ranging from 0.48 to 0.60. In pure conduction, secondary cells are non-existent; consequently, the velocity profile is a vertical. It is not the case here and this form of representation is, also, a way to propose the secondary flow. The existence of two secondary cells is pointed out on Fig. 14. Basing this profile, it is possible to evaluate the vertical dimension of a cell: in this case, the distance between the two horizontal thick lines is $Z/A = 0.066$; it means, taking into account the slot height $H = 60$ cm, that the vertical dimension of a secondary cell is of 3.95 cm. This experimental result is to bring closer to the expression (12), provided by Lee and Korpela. [6]:
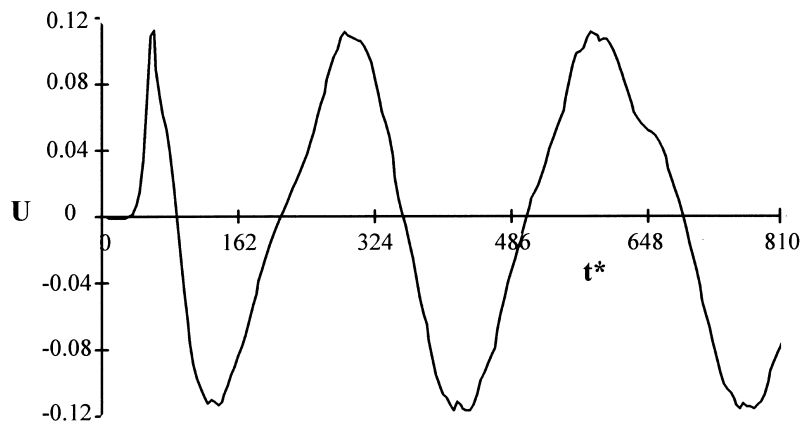
$$1_c = \left(\frac{2\pi}{\alpha_c}\right)L \tag{12}$$

Fig. 11. Evolution of dimensionless component U vs. dimensionless time t^* in the center point of a measure area.
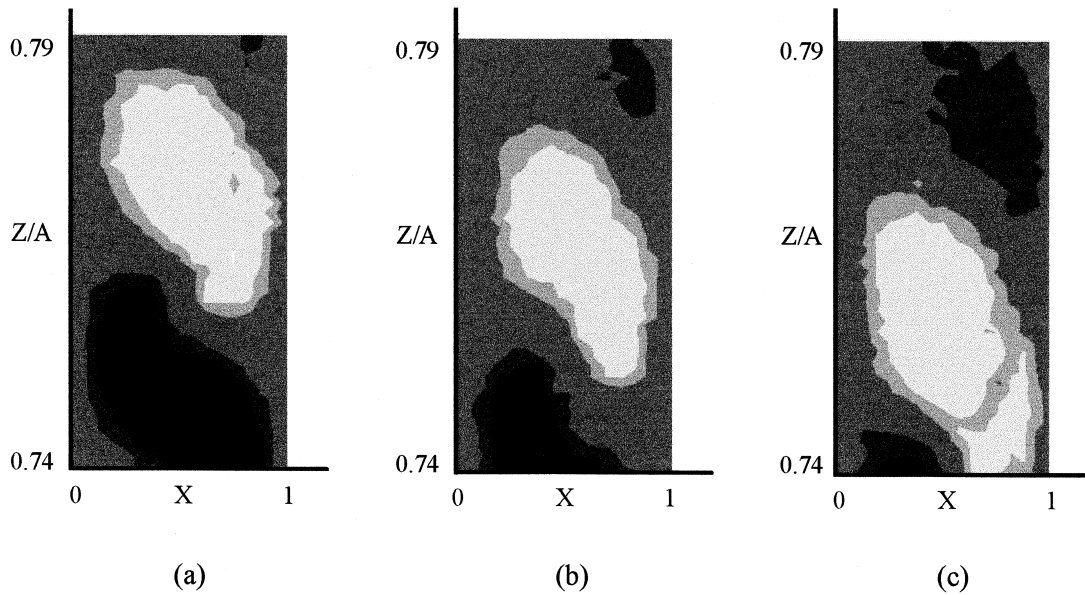
Fig. 12. Experimental non-dimensioned component U: (a) t^*, (b) $t^* + 32.4$, (c) $t^* + 64.8$.

The calculated vertical dimension of a secondary cell in the same case is there of 3.54 cm. It should be noted that this result is reached from a numerical study. Work presented here shows that expression (12) seems to be representative of reality, at least in the central zone of the cavity where the influence of the horizontal faces is not felt and where the secondary cells are fully developed.

It is possible to present an interpretation of the physical phenomenon studied. A vertical cavity of aspect ratio $A = 40$ is of very significant interest of study since this range of value corresponds to that of the double glazing whose dimensioning is partly conditioned by thermal aspect. Compared to the concrete concern of double glazing, the flow in the cavity is laminar, since the transition from laminar to turbulent
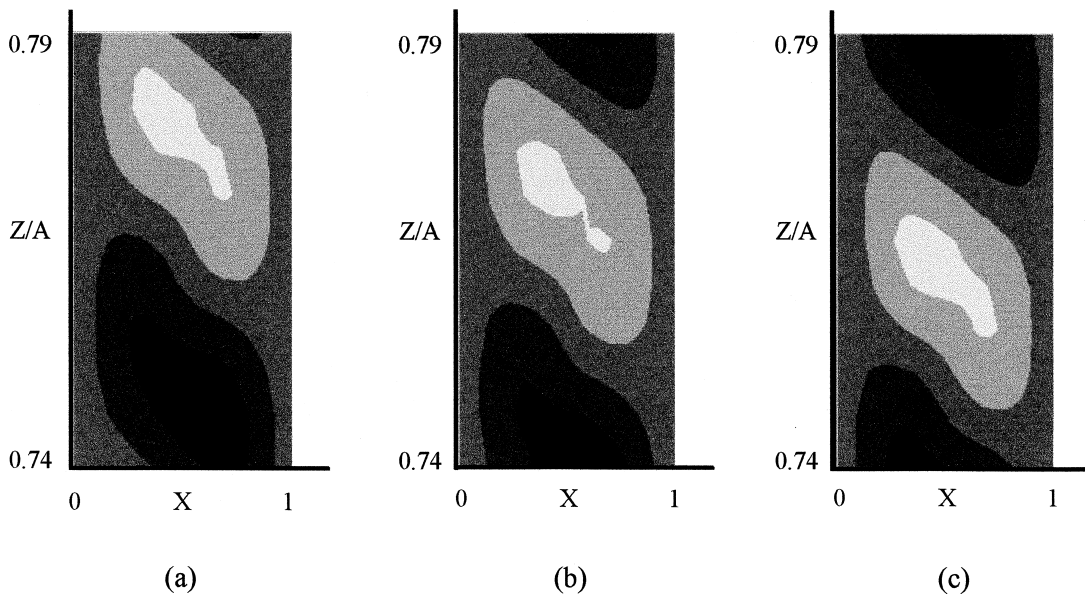

Fig. 13. Numerical non-dimensioned component U: (a) t^*, (b) $t^* + 32.4$, (c) $t^* + 64.8$.
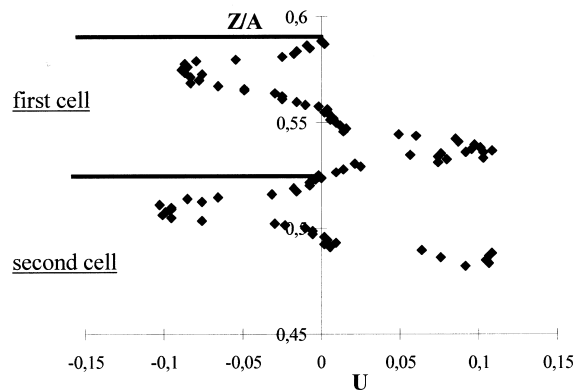
Fig. 14. Evolution of non-dimensioned horizontal velocity U vs. non-dimensioned height Z/A ($X = 0.5$ and $0.48 < Z/A < 0.60$).

flow is towards $Ra = 40{,}000$ when the aspect ratio is equal to 40 (see Fig. 1). Up to a value of 6000, the energy transfer from the hot face towards the cold face is carried out directly by conduction. If the Rayleigh number increases, conduction is not enough any more to ensure the transfer of necessary heat. The installation of a secondary flow (secondary cells) has the role to mitigate this deficit, allowing, this time, a heat transfer by convection. The results obtained tend to show that these ordered structures occur starting in the top of the cavity, for the geometrical configuration presented here. After having traversed the cavity core, each structure comes in the bottom, to be connected to the primary flow. The cells observed are ordered, actuated by an average very slow movement; the experimental as numerical results give a report of a downward flow. If the Rayleigh number increases further, these structures lose their ordered character and the flow enters the turbulent mode.

5. Conclusion

The aim of this work is to present numerical and experimental studies concerning air flow in a high aspect ratio vertical cavity. The authors put the stress on the existence of secondary flow in the cavity core using the computer code ESTET. The temperature field results provide good comparison with those available in other papers. An experimentation was implemented which allows to study the dynamic field, based on PIV technique. Secondary cells are then highlighted and velocities quantified. This paper focus moreover on the evolution of the cells in the core of the cavity: it shows that cells do not remain stationary but move downward for $A = 40$ and $Ra = 9222$. These results are obtained both with numerical and experimental study.

References

[1] A. Bejan, Convection Heat Transfer, 2nd ed., Wiley, New York, 1995.

[2] G.D. Raithby, H.H. Wong, Heat transfer by natural convection across vertical air layers, Numerical Heat Transfer 4 (1981) 447–457.

[3] G. de Vahl Davis, Laminar natural convection in an enclosed rectangular cavity, Int. J. Heat Mass Transfer 11 (1968) 1675–1693.

[4] S.A. Korpela, D. Gözum, C.B. Baxi, On the stability of the conduction regime of natural convection in a vertical slot, Int. J. Heat Mass Transfer 16 (1973) 1683–1690.

[5] J.W. Elder, Laminar free convection in a vertical slot, J. Fluid Mechanics 23 (1965) 77–98.

[6] Y. Lee, S.A. Korpela, Multicellular natural convection in a vertical slot, J. Fluid Mechanics 126 (1983) 91–121.

[7] N. Ramanan, S.A. Korpela, Multigrid solution of natural convection in a vertical slot, Numerical Heat Transfer 15 (1989) 323–339.

[8] G. Lauriat, G. Desrayaud, Natural convection in air-filled cavities of high aspect ratios: discrepancies between experimental and theoretical results, ASME Paper no. 85-HT-37, 1985.

[9] B. Roux, J. Grondin, P. Bontoux, G. de Vahl Davis, Reverse transition from multicellular to monocellular motion in vertical fluid layer, Phy. Chem. Hydro 3F (1980) 292–297.

[10] J.L. Wright, H.F. Sullivan, A two-dimensional numerical model for natural convection in a vertical rectangular window cavity, ASHRAE Transactions 100 (2) (1994) 1193–1206.

[11] P. Le Quéré, A note on multiple and unsteady solutions in two-dimensional convection in a tall cavity, ASME Journal of Heat Transfer 12 (1990) 965–974.

[12] S. Wakitani, Development of multicellular solutions in natural convection in an air-filled vertical cavity, Journal of Heat Transfer 119 (1997) 97–101.

[13] J.L. Wright, H.F. Sullivan, Natural convection in sealed glazing units: a review, ASHRAE Transactions 95 (1) (1989) 592–602.

[14] Y. Zhao, D. Curcija, W.P. Gross, Prediction of the multicellular flow regime of natural convection in fenestration glazing cavities, ASHRAE Transactions 103 (1) (1997) 1–12.

[15] S.M. ElSherbiny, G.D. Raithby, K.G.T. Hollands, Heat transfer by natural convection across vertical and inclined air layers, ASME Journal of Heat Transfer 104 (1982) 96–102.